

The Sun's Photospheric Convection Spectrum

David H. Hathaway

NASA Ames Research Center, Moffett Field, CA 94035 USA

david.hathaway@nasa.gov

Thibaud Teil

NASA Ames Research Center, Moffett Field, CA 94035 USA

thibaud.teil@gmail.com

Aimee A. Norton

W.W. Hansen Experimental Physics Laboratory, Stanford University, Palo Alto, CA 94305 USA

aanorton@stanford.edu

Irina Kitiashvili

NASA Ames Research Center, Moffett Field, CA 94035 USA

irina.n.kitiashvili@nasa.gov

ABSTRACT

Spectra of the cellular photospheric flows are determined from full-disk Doppler velocity observations acquired by the Helioseismic and Magnetic Imager (HMI) instrument on the Solar Dynamics Observatory (SDO) spacecraft. Three different analysis methods are used to separately determine spectral coefficients representing the poloidal flows, the toroidal flows, and the radial flows. The amplitudes of these spectral coefficients are constrained by simulated data analyzed with the same procedures as the HMI data. We find that the total velocity spectrum rises smoothly to a peak at a wavenumber of about 120 (wavelength of about 35 Mm), which is typical of supergranules. The spectrum levels off out to wavenumbers of about 400, and then rises again to a peak at a wavenumber of about 3500 (wavelength of about 1200 km), which is typical of granules. The velocity spectrum is dominated by the poloidal flow component (horizontal flows with divergence but no curl) at wavenumbers above 30. The toroidal flow component (horizontal flows with curl but no divergence) dominates at wavenumbers less than 30. The radial flow velocity is only about 3% of the total flow velocity at the lowest wavenumbers, but increases in strength to become about 50% at wavenumbers near 4000. The spectrum compares well with the spectrum of giant cell flows at the lowest wavenumbers and with the spectrum of granulation from a 3D radiative-hydrodynamic simulation at the highest wavenumbers.

Subject headings: convection, Sun: granulation, Sun: interior, Sun: photosphere

1. INTRODUCTION

The Sun is the only star for which we can directly observe the convective motions that carry energy from its radiative interior to its photo-

sphere. While buoyancy and heat transport drive these motions, these flows also transport magnetic field and angular momentum and thus play a critical role in the rotational and magnetic history of the star. The convective motions, and their in-

teractions with magnetic fields, are the ultimate drivers behind many scientific questions concerning the Sun — what is the source of the 11-year sunspot cycle, what heats the Sun’s corona, what accelerates the solar wind, what triggers solar flares, prominence eruptions, and coronal mass ejections?

Solar granules, bright cells with darker borders, were observed with solar telescopes by the 1860s. These cellular flows have diameters of about 1Mm, flow speeds of about 3000 m s^{-1} , and lifetimes of about 10 minutes (Bray et al. 1984).

The much larger supergranules were first noticed by Hart (1954) but named and better characterized by Leighton et al. (1962). Supergranules have diameters of about 35 Mm, flow speeds of about 400 m s^{-1} , and lifetimes of about a day (Rieutord & Rincon 2010).

Even larger cells, giant cells, were proposed to exist based on theoretical arguments (Simon & Weiss 1968). Hints of the possible existence of these cells have been uncovered over the ensuing decades but detailed observations and characterizations have only come recently (Hathaway et al. 2013). These cells have widths of 100 Mm or more, flow speeds of about 10 m s^{-1} , and lifetimes of several months.

Yet another set of cells, mesogranules, were found by November et al. (1981) to be intermediate in size, flow speeds, and lifetimes between granules and supergranules.

The advent of space based observations, with both continuous coverage and high spatial and temporal resolution, has enabled many new studies of solar convection. Data from the Michelson Doppler Investigation (MDI) on the ESA/NASA Solar and Heliospheric Observatory (SOHO) mission were analyzed by several groups. Lawrence et al. (1999) used a wavelet analysis on Doppler, intensity, and magnetic images. They noted that granules dominated the radial flows while supergranules dominated the horizontal flows, but mesogranules were notably weak. (They also concluded that their wavelet analysis only captured about 30% of the signal.) The MDI Doppler data were analyzed and simulated by Hathaway et al. (2000) to obtain photospheric kinetic energy spectra covering spherical harmonic wavenumbers, ℓ , from $\ell \sim 1$ to $\ell \sim 3000$. They concluded that only two spectral features were

evident, a peak representing supergranules at $\ell \sim 120$ and a broad peak representing granules at $\ell > 1000$. Others (e.g. Rieutord et al. 2000) have also concluded that mesogranulation is not a true or discrete scale of solar convection.

Power spectra of the flows at very high wavenumbers were obtained by Rieutord et al. (2010) from high resolution images obtained with the Solar Optical Telescope (SOT) on the *Hinode* spacecraft. Their horizontal flow spectra show a prominent peak in power at wavenumbers typical for supergranules, along with a continuum of power out to higher wavenumbers. (Their correlation tracking method for measuring the horizontal flows limited their measurements to cells larger than ~ 2.5 Mm or $\ell \sim 1800$.) Their vertical flow spectra (obtained from Doppler velocity measurements) show a prominent peak in power at wavenumbers typical of granules ($\ell \sim 2500$) with a rapid fall off at higher wavenumbers.

Here we investigate the Sun’s photospheric convection spectrum by analyzing Doppler data from the HMI instrument. These data have much higher spatial resolution, and better instrumental characterization, than the MDI data. The higher resolution data gives better confidence in characterizations of the high-wavenumber flow structures. The better characterization of the HMI instrument, its imaging artifacts, and its point-spread-function, gives better confidence in the characterizations at both ends of the spectrum.

We employ a new Doppler data analysis tool to determine the toroidal component of the horizontal flows (vortical flows with curl but no divergence). While the short (compared to the 27-day solar rotation period) lifetimes of supergranules suggest that solar rotation should not be a big influence on the flows, numerical simulations (Hathaway 1982) and observations (Duvall & Gizon 2000) indicate that the flows in supergranules have a preferred sense of vorticity in each hemisphere. This tendency should be stronger for the larger, slower cellular flows.

In the following section we describe the data and the data preparation. These data directly measure only the line-of-sight velocity component and only over the visible hemisphere. We analyze the data with three different analysis methods in an effort to separate the Doppler signal into three components associated with the full vector veloc-

ities in the convective flows. In order to fully, and accurately, quantify the vector velocities we construct simulated data in which we know the actual vector velocities over the entire solar surface. The simulated data are then run through the same analysis procedures, results are compared with those from the HMI data, and the simulated data are then revised until a match is obtained.

This data simulation is described in Section 3. The Doppler velocity spherical harmonic spectrum analysis is described in Section 4. An analysis that separates the radial flow component from the horizontal flow component is described in Section 5. An analysis that separates poloidal flows (diverging horizontal flows) from toroidal flows (horizontal flow vortices) is described in Section 6. The full spectrum of motions for all flow components is presented in the concluding section along with comparisons to the spectrum from a numerical simulation of the smallest length scales, and to the spectrum of giant cell flow velocities from the correlation tracking method described in Hathaway et al. (2013).

2. DATA PREPARATION

The data used in this study consist of line-of-sight Doppler velocities measured by the HMI instrument (Scherrer et al. 2012) on the SDO spacecraft. These 4096-by-4096 pixel images are obtained every 45 seconds and then averaged over 720 seconds to remove the 5-minute p -mode oscillation signal. Schou et al. (2012) and Couvidat et al. (2012) describe the data acquisition and calibration procedures. The Doppler velocity is calculated from the intensity measured at six different spectral tuning positions around the wavelength of the selected Fe I absorption line at 6173 Å. An example of a data image is shown in Figure 1.

Our first step is to remove the velocity signal due to the motion of the spacecraft and the velocity artifacts associated with the instrument itself. Using the spacecraft velocity relative to the Sun still leaves behind diurnal signals clearly associated with the spacecraft’s geosynchronous orbit. We found that these variations alter the artifact signal as a function of spacecraft velocity toward or away from the Sun. The artifacts also change when the instrument focus is changed. To mini-

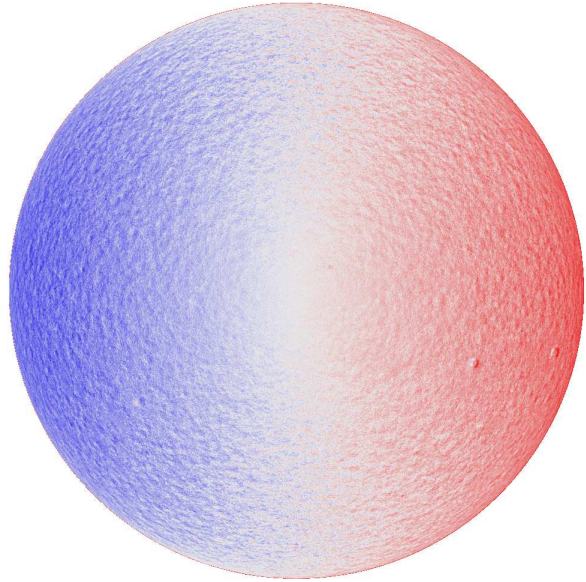


Fig. 1.— Doppler velocity image from the SDO/HMI instrument for November 1, 2012 at 5:00UT. The line-of-sight velocity signal ranges from -3000 m s^{-1} (dark blue) to $+3000 \text{ m s}^{-1}$ (dark red). The signal is dominated by the $\pm 2000 \text{ m s}^{-1}$ signal from the Sun’s rotation but the mottled pattern produced by the solar convection is also very apparent (as are “blemishes” due to flows around sunspots).

mize the impact of these variations on our results, we chose data taken when the spacecraft motion toward or away from the Sun was less than 300 m s^{-1} (one tenth of the $\pm 3000 \text{ m s}^{-1}$ daily range).

We extract the imaging artifacts by first removing the large-scale solar velocity signals that are fixed in the image (e.g. the Doppler signal due to the axisymmetric flows, the gravitational red shift, and the convective blue shift). We then average over many hundreds of images so that the signal due to the more or less random convective flows cancel as they evolve and rotate across the visible disk while the artifacts remain fixed. The artifact image obtained from data acquired between the dates of October 1, 2012 and May 31, 2013 is shown in Figure 2. These artifacts would introduce spurious features at low spatial wavenumbers in our spectral analyses.

For this study we have analyzed data acquired in November 2012. After removing the Doppler

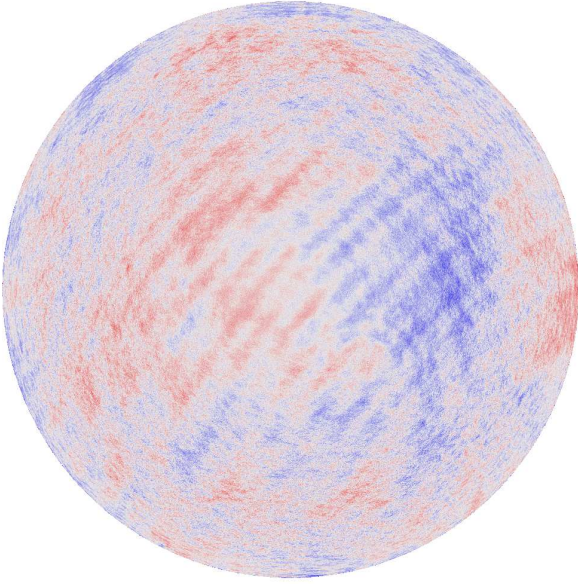


Fig. 2.— Doppler velocity image showing imaging artifacts from the SDO/HMI instrument for October 2012 through May 2013. The line-of-sight velocity signal ranges from -150 m s^{-1} (dark blue) to $+150 \text{ m s}^{-1}$ (dark red).

signals due to the spacecraft motion and the imaging artifacts, each Doppler image is analyzed using the procedures described in Hathaway (1987) and Hathaway (1992) to measure and remove the Doppler signals due to the axisymmetric flows (differential rotation and the meridional circulation) and the signal due to the convective blue shift.

The convective blue shift is an apparent flow toward the observer caused by the correlation between radial upflows and emergent radiative intensity in the unresolved convective flows (granules). (The Doppler velocity is an intensity weighted average over the flow structures within a pixel.) It varies systematically from disk center to limb as the line-of-sight samples different velocity components and different levels of the solar atmosphere. The convective blue shift changes substantially in regions where magnetic fields thread through the surface. Therefore, the convective blue shift signal requires additional corrections. Figure 3 shows the convective blue shift signal for both field free regions and for regions with varying magnetic flux density. (Note that while a 636.4 m s^{-1} gravitational red shift has been subtracted from the

signal, the original zero point was arbitrarily set to make the data median match the spacecraft's radial velocity.) The convective blue shift is substantially altered in magnetic areas. Uncorrected, this introduces Doppler signals that are not directly related to actual flows on the Sun's surface.

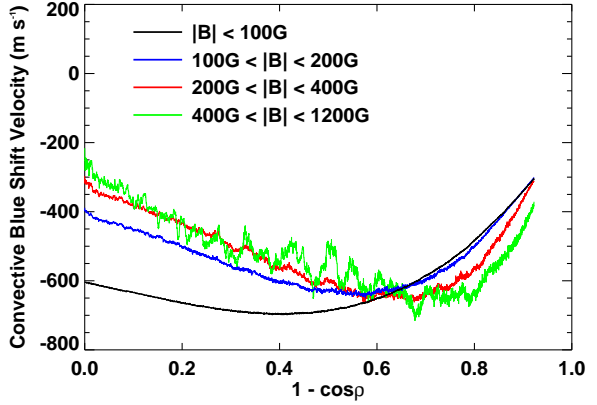


Fig. 3.— The convective blue shift signal from the SDO/HMI instrument for regions free of magnetic field (black line) and regions with radial magnetic flux density from 100 to 200 G (blue line), 200 to 400 G (red line), and 400 to 1200 G (green line).

We fit the convective blue shift signal, $CBS(x)$, to shifted Legendre polynomials (polynomials orthonormal with uniform weights on the interval $0 \leq x \leq 1$) with the dependent variable

$$x = 1 - \cos \rho \quad (1)$$

where ρ is the heliocentric angle of a point from disk center. The first five shifted Legendre polynomials are:

$$P_0^*(x) = 1 \quad (2)$$

$$P_1^*(x) = \sqrt{3}(2x - 1) \quad (3)$$

$$P_2^*(x) = \sqrt{5}(6x^2 - 6x + 1) \quad (4)$$

$$P_3^*(x) = \sqrt{7}(20x^3 - 30x^2 + 12x - 1) \quad (5)$$

$$P_4^*(x) = 3(70x^4 - 140x^3 + 90x^2 - 20x + 1) \quad (6)$$

We find that the convective blue shift signal is well fit with these first five polynomials such that

$$CBS(x) = \sum_{n=0}^4 C_n P_n^*(x) \quad (7)$$

The fit coefficients for the different magnetic flux densities are given in Table 1.

Flux Density	C_0	C_1	C_2	C_3	C_4
< 100	-584	105	92	19	0
$[100, 200]$	-508	35	113	37	3
$[200, 400]$	-490	-4	123	59	15
$[400, 1200]$	-497	-35	102	71	33

Table 1: Convective blue shift fit coefficients (in units of m s^{-1}) for increasing magnetic flux density (in units of Gauss).

We correct the data for the convective blue shift differences in magnetic regions and find that a single convective blue shift signal, shown in Figure 4, represents all the data. We then subtract this signal from the data.

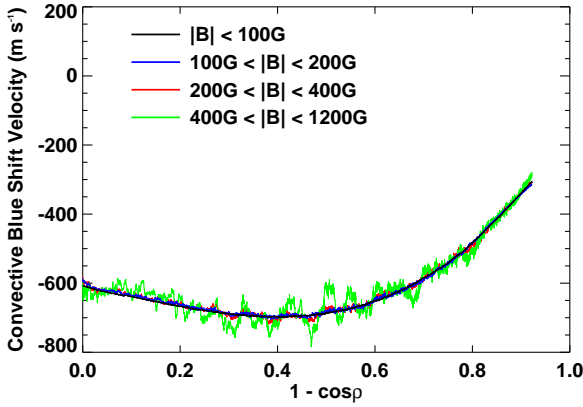


Fig. 4.— The convective blue shift signal after correcting for magnetic effects. The four lines represent regions free of magnetic field (black line) and regions with radial magnetic flux density from 100 to 200 G (blue line), 200 to 400 G (red line), and 400 to 1200 G (green line).

After removing these signals (the convective blue shift, the artifacts, the Doppler signal due to differential rotation and meridional flow) the Doppler data are dominated by the signal from the line-of-sight velocities in the cellular flows. A

example of these corrected data is shown in Figure 5.

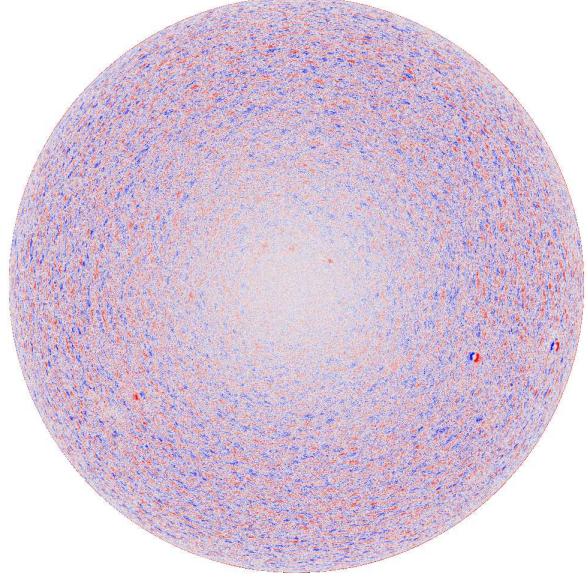


Fig. 5.— Prepared Doppler velocity image from the SDO/HMI instrument for November 1, 2012 at 5:00UT. The line-of-sight velocity signal ranges from -1000 m s^{-1} (dark blue) to $+1000 \text{ m s}^{-1}$ (dark red).

3. THE DATA SIMULATION

We produce simulated data (for which we know the full vector velocities over the entire surface of the Sun) that faithfully reproduce the HMI Doppler data.

We represent the vector velocity field on the surface of a sphere by a spectrum of poloidal and toroidal modes (Chandrasekhar 1961) with

$$V_r(\theta, \phi) = \sum_{\ell=0}^{\ell_{max}} \sum_{m=-\ell}^{\ell} R_{\ell}^m Y_{\ell}^m \quad (8)$$

$$V_{\theta}(\theta, \phi) = \sum_{\ell=1}^{\ell_{max}} \sum_{m=-\ell}^{\ell} \left[S_{\ell}^m \frac{\partial Y_{\ell}^m}{\partial \theta} + T_{\ell}^m \frac{1}{\sin \theta} \frac{\partial Y_{\ell}^m}{\partial \phi} \right] \quad (9)$$

$$V_{\phi}(\theta, \phi) = \sum_{\ell=1}^{\ell_{max}} \sum_{m=-\ell}^{\ell} \left[S_{\ell}^m \frac{1}{\sin \theta} \frac{\partial Y_{\ell}^m}{\partial \phi} - T_{\ell}^m \frac{\partial Y_{\ell}^m}{\partial \theta} \right] \quad (10)$$

where $Y_\ell^m(\theta, \phi)$ is a spherical harmonic function of degree ℓ and azimuthal order m , θ is the colatitude measured southward from the north pole, and ϕ is the azimuth measured prograde from the central meridian. The complex coefficients R_ℓ^m , S_ℓ^m , and T_ℓ^m are the spectral coefficients for the radial, poloidal, and toroidal components, respectively.

We simulate the observed line-of-sight velocity by specifying these complex spectral coefficients for all spectral components up to a maximum spherical harmonic degree, $\ell_{max} = 4096$. This is an iterative, trial and error, process in which spectral amplitudes are prescribed, simulated data are constructed and analyzed, the results are compared to those from the HMI data, and new spectral coefficients are constructed based on those comparisons. We start with an estimate of the spectral amplitudes as functions of ℓ . The complex coefficients for each azimuthal order, m , use these spectral amplitudes but with random phases for the real and imaginary parts. We use the same phase for the radial and poloidal spectral coefficients since these two components are linked through the mass continuity equation ($\nabla \cdot v = 0$) with

$$\ell(\ell+1)S_\ell^m = \frac{1}{r} \frac{\partial}{\partial r} [r^2 R_\ell^m(r)] \quad (11)$$

We do not link the phase of the toroidal component to the other two.

We calculate the three vector velocity components from this spectrum at an array of points with 4096 points equi-spaced in θ and 8192 points equi-spaced in ϕ . We then project these vector velocities onto the line-of-sight at each pixel in a 4096-by-4096 image of the solar disk as seen from 1 AU. The average Doppler velocity in each pixel is calculated by finding the line-of-sight projection at a 7-by-7 array of sub-pixels using bi-cubic interpolation from points on the vector velocity grid and then averaging over those sub-pixels that are on the visible disk.

The line-of-sight velocity at a point (θ, ϕ) is given by

$$\begin{aligned} V_{los}(\theta, \phi) = & V_r(\theta, \phi) [\sin B_0 \cos \theta + \cos B_0 \sin \theta \cos \phi] + \\ & V_\theta(\theta, \phi) [\sin B_0 \sin \theta - \cos B_0 \cos \theta \cos \phi] + \\ & V_\phi(\theta, \phi) [\cos B_0 \sin \phi] \end{aligned} \quad (12)$$

where B_0 is the latitude at disk center (or equivalently the tilt of the Sun's north pole toward the observer) and velocities away from the observer are taken to be positive.

We also add, at each pixel, a convective blue shift signal that is a function of the heliocentric angle from disk center. This signal complicates the extraction of the Doppler signal due to the meridional flow. If these flows are not properly characterized and removed, they leave behind large-scale Doppler signals that impact the spectrum at low wavenumbers. By also including this “fictitious” signal we faithfully reproduce the full data and analysis associated with the HMI data.

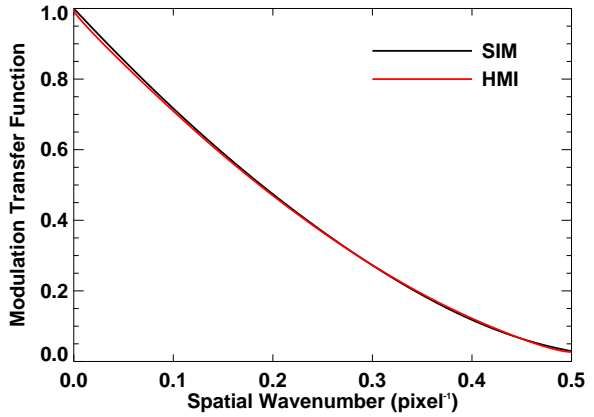


Fig. 6.— The modulation transfer function (MTF) for the HMI instrument (red line) and the functional fit used for the simulation (black line).

A point-spread-function (PSF) was developed to remove stray light from HMI data and is used here in the data simulation. First, a modulation transfer function (MTF) was obtained from ground-based calibration data using field stops (Wachter et al. 2012) in order to describe the pre-launch instrumental optics. We fit the MTF with an exponential convolved with the ideal optical transfer function (OTF), often known as a ‘chat’ function. The exponential and ‘chat’ function in the frequency domain are equivalent to a Lorentzian and Airy function in the spatial domain. Post-launch data including solar aureole, lunar eclipse and Venus transit events were used to evaluate how well the PSF was able to reproduce the observed scattering.

The final value of gamma (the wavenumber ex-

ponent) in the exponential function was determined through least squares fitting of the transit of Venus data on 2012.06.05 from the side camera data. The final, non-ideal form of the MTF and subsequent PSF was further modified for the following reasons. Lunar eclipse images, where a large portion of the solar image is obscured by the lunar disk, enabled a measure of the large-scale scattering. One such eclipse occurred on 2010.10.07 and the HMI continuum intensity filtergram shows a light level of 0.34% of the disk-center continuum intensity for a position 200 pixels onto the lunar disk. We found that the light level tended towards a constant far away instead of continually decreasing with increasing distance from the solar limb. This motivated an additional term to be added to the PSF to fit the tail of the distribution. If we only considered light scattered from $10''$ away then the additional term would not be necessary, meaning that using only the Venus transit data was not sufficient in order to emulate the large-scale scattering/dust on the optics. (Note that the PSF we developed differs from previous stray light removal efforts since we do not use a single Gaussian or sum of Gaussians as the central mathematical component.)

Deconvolved images were compared to the originals and it was found that the minimum intensity of a sunspot umbrae decreased from being 5.5% of the nearby quiet-Sun continuum intensity in the original image to being 3.3% in the deconvolved image while the granulation contrast doubled, with a standard deviation of the intensity in the quiet-Sun being 3.7% of the average in the original image and 7.2% of the average in the deconvolved image.

In our data simulation we average the line-of-sight velocity over all sub-pixels within a pixel that fall on the visible disk of the Sun and then convolve that image with the PSF found for the HMI instrument. This convolution is implemented by multiplying the FFT of the image with the FFT of the PSF (the MTF) and then performing an inverse FFT on the result. The MTF found for HMI is shown in Figure 6 along with the functional fit (which is what we actually use) given by

$$MTF(k) = \exp(-k^5)(1 - k/2)^3 \sin(k\pi/2)/(k\pi/2) \quad (13)$$

An example of a Doppler image from the data simulation after the signals due to the axisymmetric flows and the convective blue shift are removed is shown in Figure 7.

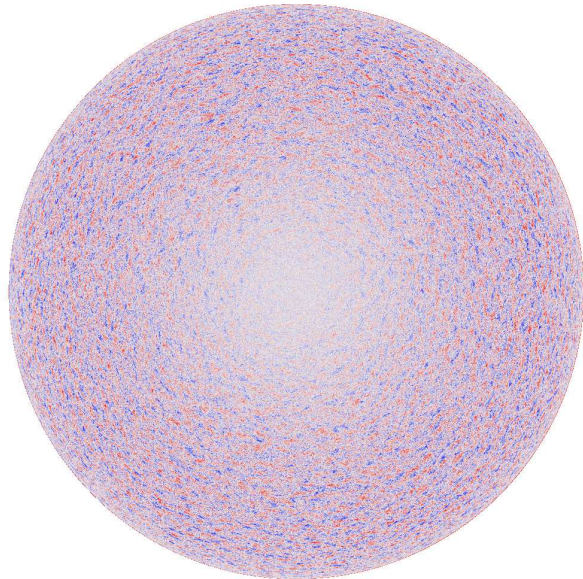


Fig. 7.— Simulated Doppler velocity image. The line-of-sight velocity signal ranges from -1000 m s^{-1} (dark blue) to $+1000 \text{ m s}^{-1}$ (dark red).

4. DOPPLER VELOCITY SPECTRUM

We calculate Doppler velocity spectra following Hathaway et al. (2000). We remove active regions in the HMI data by locating pixels where the magnetic flux density exceeds 1200 G and then masking out those pixels along with all adjacent pixels within a 10 pixel radius. The full disk HMI data, its mask, and the simulated data are projected onto maps in heliographic longitude and latitude. The mask edges are smoothed by convolving the mask with a cosine bell having a radius of 10 pixels. The masked data is then projected onto spherical harmonics by taking Fourier transforms in longitude and Legendre transforms in latitude to obtain complex spectral coefficients, A_ℓ^m , that reproduce the masked data when multiplied by the spherical harmonics and summed over ℓ and m .

The HMI data are comprised of 59 Doppler images acquired during November 2012 at the hourly intervals when the spacecraft motion toward or away from the Sun was less than 300 m s^{-1} . The

simulated data are comprised of 18 Doppler images constructed with different sets of random numbers for the spectral phases. The average velocity spectra are shown in Figure 8.

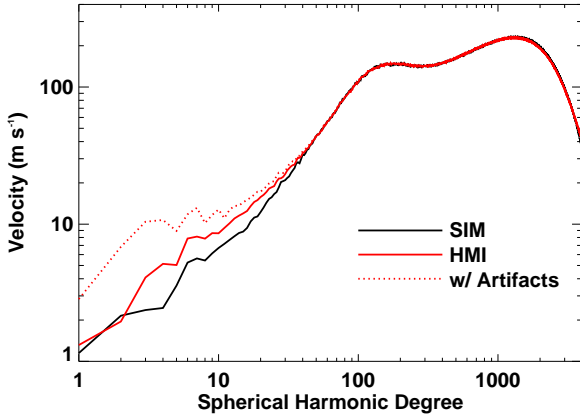


Fig. 8.— The Doppler velocity spectra for the simulated data (black line) and the HMI data (red line). The dotted red line shows the spectrum obtained from the HMI data when the artifacts are not removed.

These spectral values are calculated by taking the square root of the wavenumber times the velocity power per wavenumber:

$$V(\ell) = \sqrt{\ell \sum_{m=-\ell}^{\ell} |A_{\ell}^m|^2} \quad (14)$$

The Doppler velocity spectrum rises to a peak at $\ell \sim 120$ (consistent with typical supergranules with diameters of ~ 35 Mm), drops slightly and then rises again to a second peak at $\ell \sim 3500$ (consistent with granules with diameters of ~ 1.2 Mm).

Note that this spectrum is for the Doppler velocities. It includes foreshortening at the limb, which limits the signal at high wavenumbers, and it includes line-of-sight effects, which exclude horizontal velocities at disk center and only include one horizontal velocity component across the rest of the disk. In spite of these caveats, it is nonetheless clear that the spectrum is continuous with only two primary features — peaks representative of granules and supergranules.

While cells of all sizes are included, there isn't a spectral feature that indicates a preference for

mesogranules of any particular size. The bottom of the spectral dip at $\ell \sim 400$ represents cells with diameters of ~ 10 Mm — a quoted size for mesogranules.

We have forced the simulation spectrum to drop smoothly at low wavenumbers. While this leaves an apparent excess of power in the HMI data at wavenumbers below 30, we attribute this signal excess to a less than perfect removal of the image artifacts. This is supported by the low wavenumber feature seen in the data when the artifacts are not removed (dotted red line in Figure 8).

5. RADIAL FLOW ANALYSIS

The radial flow component represented by R_{ℓ}^m can be separated from the horizontal flow components using the method described by Hathaway et al. (2002). The Doppler velocity due to the horizontal flows drops to zero at disk center, where all horizontal velocities are transverse to the line-of-sight, while the radial velocity has its strongest contribution to the Doppler signal at disk center.

The line-of-sight velocity is given by

$$V_{los}(\theta, \phi) = V_r(\theta, \phi) \cos \rho + V_{h1}(\theta, \phi) \sin \rho \quad (15)$$

where V_{h1} is the component of the horizontal flow velocity aligned with the radius vector from disk center, and ρ is the heliocentric angle from disk center. The orthogonal component of the horizontal flow is transverse to the line-of-sight and does not contribute to the Doppler signal. Squaring the Doppler velocity and averaging it in annuli about disk center at a given ρ gives

$$\overline{V_{los}^2(\rho)} = \overline{V_r^2} \cos^2 \rho + \overline{V_{h1}^2} \sin^2 \rho + \frac{2\overline{V_r V_{h1}} \cos \rho \sin \rho}{\quad} \quad (16)$$

where the overbars represent the averages. We expect the last term in this equation to be negligible. There is no physical or geometric reason that $V_r V_{h1}$ should have a nonzero average on an annulus. For example, the up flow at the center of a cell should produce horizontal flows away from disk center on one side and toward disk center on the other — giving a net zero average. Dropping this term, we rewrite the equation as

$$\overline{V_{los}^2}(\rho) = \overline{V_r^2} + [\overline{V_{h1}^2} - \overline{V_r^2}] \sin^2 \rho \quad (17)$$

This suggests a method for separating the radial flow from the horizontal flow component in the Doppler velocity signal. If we plot the average Doppler velocity squared as a function of $\sin^2 \rho$, then the y-axis intercept gives the radial velocity squared and the slope gives the difference between the square of the horizontal component and the square of the radial component.

We need to know the contributions to the Doppler signal from the radial and horizontal flows as functions of wavenumber. To do so we reconstruct the Doppler signal from the spherical harmonic spectral coefficients, A_ℓ^n , multiplied by spectral filters to isolate Doppler features of different sizes. We chose a set of Gaussian filters of width $\Delta\ell = 64$ centered on multiples, n , of $\ell = 128$ from $\ell = 0$ to $\ell = 4096$ with

$$Filter_n(\ell) = \exp[-(\ell - n128)^2 / (2\Delta\ell^2)] \quad (18)$$

The average Doppler velocity squared for each of these 33 filtered Doppler images is fit to a second order polynomial in $\sin^2 \rho$ (foreshortening away from disk center introduces curvature to these data). The y-axis intercept yields the radial flow velocity squared while the slope yields the difference between the squared radial and squared horizontal flow velocities. The radial flow components are shown in Figure 9 as functions of ℓ for both the HMI and the simulated data. The ratios of the radial flow component to the horizontal flow component are shown in Figure 10 as functions of ℓ for both the HMI and the simulated data.

Note that this analysis compares the radial flow velocity to just one component of the horizontal flow velocity. While it is clear that the radial flow is very weak at low wavenumbers and becomes comparable to the horizontal flows at large wavenumbers, a quantitative value is best obtained from the vector velocities in the simulation.

The simulation has radial flow velocities that are just 3% of the total flow velocity at the lowest wavenumbers ($\ell \sim 10$). This ratio rises to 6% at supergranule wavenumbers ($\ell \sim 120$) and to 45% at granule wavenumbers ($\ell \sim 4000$).

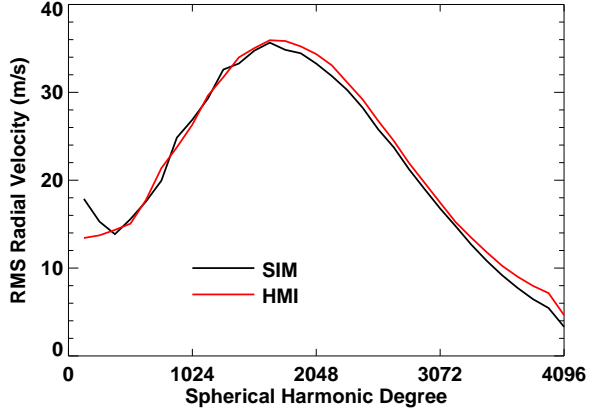


Fig. 9.— The radial flow component of the Doppler velocity for the simulated data (black line) and the HMI data (red line).

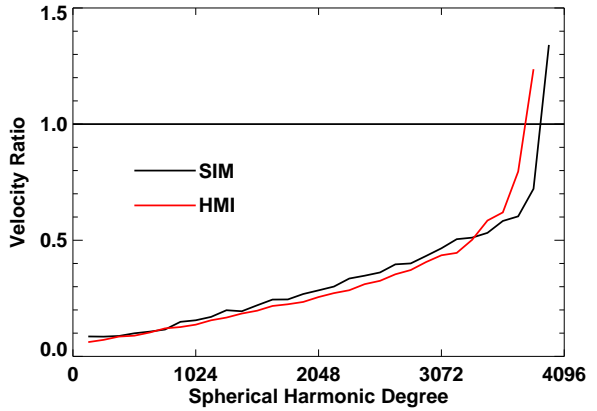


Fig. 10.— The ratio of the radial flow component to the horizontal flow component of the Doppler velocity for the simulated data (black line) and the HMI data (red line).

6. TOROIDAL/POLOIDAL FLOW ANALYSIS

We have devised a new analysis technique to separate the toroidal flow component from the poloidal flow component. We construct two velocity gradient images from the prepared data by calculating the pixel-wise gradient of the Doppler velocity (a scalar) at each point in the image and finding the projection of that gradient in the disk-radial direction (from disk center toward the limb) to produce one image (the Grad_ρ image) and the projection of the gradient in the tangential direction (clockwise about disk center) to produce the

second image (the Grad_Θ image).

A poloidal flow away from a convection cell center will contribute to the Grad_ρ image but not to the Grad_Θ image along lines that pass radially and tangentially through the cell center. Likewise, a toroidal flow around the center of a vortex anywhere on the disk will contribute to the Grad_Θ image but not to the Grad_ρ image along these same lines. Unfortunately, a radial flow will contribute to both images and both poloidal and toroidal flows will contribute to both images away from the lines that pass through cell centers in the radial and tangential directions. While the separation into poloidal and toroidal components is not clean and simple, the data simulation allows us to nonetheless quantify the contributions of these flows to the Grad_ρ and Grad_Θ images.

We produce these Grad_ρ and Grad_Θ images for both the HMI and the simulated data and then find their spherical harmonic spectral coefficients using the same procedure used for the Doppler velocity spectrum in Section 4.

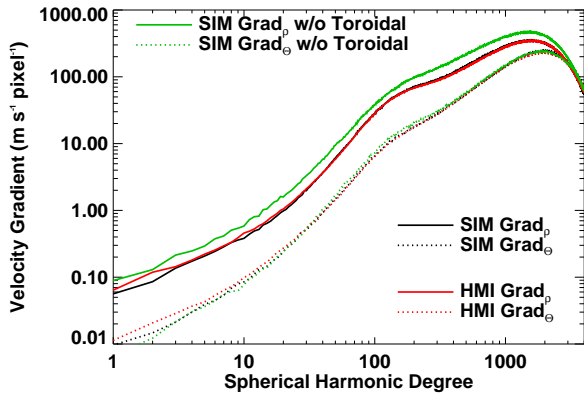


Fig. 11.— The spectra from the Grad_ρ images (solid lines) and Grad_Θ images (dotted lines) for the simulated data with both poloidal and toroidal flows (black lines), the HMI data (red lines), and the simulated data in which the horizontal flows are purely poloidal without a toroidal component (green lines).

The results are shown in Figure 11. We illustrate the sensitivity of the method to poloidal and toroidal flows using two simulations. Both simulations have horizontal flows that produce the spectral match shown in Figure 8 and radial flows that produce the spectral matches shown

in Figures 9 and 10. One simulation, shown in black in Figure 11, has both poloidal and toroidal flows adjusted to match the HMI Grad_ρ and Grad_Θ spectra (shown in red). The second simulation (shown in green), has only poloidal flows without a toroidal flow component. The excess velocity at all wavenumbers in the Grad_ρ image spectrum from this simulation indicates that a substantial fraction of the observed horizontal flows must be toroidal. The deficient velocity at wavenumbers below $\ell \sim 30$ in the Grad_Θ image spectrum from this simulation suggests that the toroidal flows dominate at these lower wavenumbers.

7. CONCLUSIONS

As a result of these analyses, we have simulated flows that closely reproduce the analysis results from the HMI data seen in the spectral matches in the previous sections. The simulations require prescribing all three spectral coefficients (radial, poloidal, and toroidal) for all wavenumbers from 1 to 4096. The total velocity spectrum and its three components are plotted in Figure 12 as functions of spherical harmonic degree ℓ . Note that these spectra are from the vector velocities over the entire solar surface and that they are not impacted by the foreshortening or line-of-sight projection effects that impact the spectra from the Doppler images.

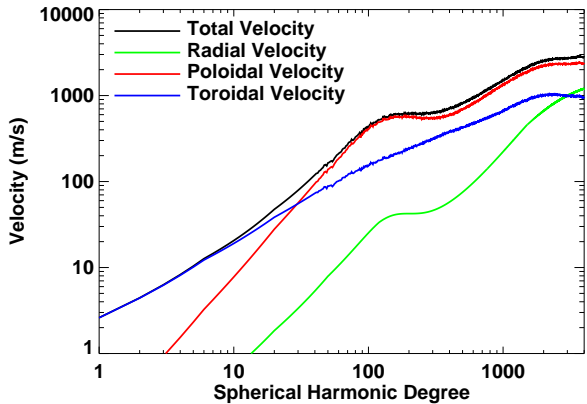


Fig. 12.— The total velocity spectrum (black line) from the data simulation. The contribution from the poloidal flow is shown in red. The contribution from the toroidal flow is shown in blue. The contribution from the radial flow is shown in green.

As with the Doppler Velocity spectrum, we see

that the total velocity spectrum rises to the peak at $\ell \sim 120$, consistent with supergranules, drops slightly at higher wavenumbers and then rises to the second peak at $\ell \sim 3500$, consistent with granules. The two velocity components coupled by the mass continuity equation, the radial and poloidal components, have pronounced peaks consistent with supergranules while the toroidal component does not.

None of the components show any spectral features indicating a preferred cell size at the lowest wavenumbers representing giant cells or at the intermediate wavenumbers representing mesogranules.

We conclude that, in general, the convection spectrum is a rising spectrum with velocities increasing linearly (slope of ~ 1 on this log-log plot) with wavenumber ℓ to an ultimate peak at wavenumbers of $\ell \sim 3500$ consistent with the photospheric granulation. However, this linear rise is punctuated by a peak at $\ell \sim 120$ consistent with supergranules.

The origin of this supergranule peak is still uncertain. Simon & Leighton (1964) suggested that cells the size of supergranules are driven by the changes in mean molecular weight at depths where helium becomes ionized (depths of ~ 7 Mm for the first ionization of He and ~ 30 Mm for the second ionization of He). November et al. (1981) isolated mesogranule-sized cells and suggested that mesogranules were driven by the first ionization of He and supergranules by the second ionization of He. Rast (2003) suggested that cells the size of mesogranules and supergranules would be driven by the collective interactions between downdrafts at cell boundaries. However, radiative-MHD simulations of convection in the outer 20 Mm of the Sun by Stein et al. (2011) include all of these processes, but do not yield any dominant cells sizes in the photosphere other than granules. (These simulations do, however, indicate that the smaller structures disappear in deeper layers, leaving velocity structures with sizes proportional to the depth.)

The relative strength of the radial flow velocity to the total flow velocity increases from 3% at the lowest wavenumbers to nearly 50% at the highest wavenumbers. This is in rough agreement with the results found with the lower resolution MDI data by Hathaway et al. (2002), but extends the results to much higher wavenumbers, and slightly lowers

the radial flow velocities at the lowest wavenumbers (where imaging artifacts were removed from the HMI data).

The toroidal flow component dominates at low wavenumbers and becomes comparable to the poloidal component at $\ell \sim 30$, where velocities of $\sim 70 \text{ m s}^{-1}$ and cell sizes of ~ 150 Mm give a characteristic time scale of ~ 24 days — comparable to the Sun’s rotation period.

The spectrum shown in Figure 12 is derived from Doppler velocity data obtained with HMI. This spectrum can be compared to spectra obtained by other means.

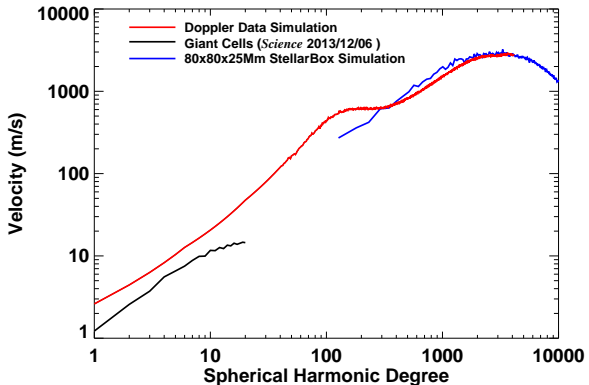


Fig. 13.— The total velocity spectrum (red line) from the data simulation is plotted for comparison with the spectrum from the vector velocities found for giant cells (Hathaway et al. 2013) and the spectrum from the vector velocities in the StellarBox simulation of solar granulation.

Hathaway et al. (2013) measured the giant cell sized flows by a local correlation tracking method on the Doppler velocity features (largely supergranules). This analysis produced maps of the horizontal vector velocities for all solar longitudes and most solar latitudes (the extreme polar regions were inaccessible). The velocity spectrum averaged over 34 solar rotations from May 2010 through November 2012 is shown in Figure 13 by the black line at low wavenumbers. The giant cell flow velocities are somewhat smaller than those in our simulation, but the slope agrees very well. Our data simulation may overestimate the velocity at these low wavenumbers by having to fit to HMI data that is still impacted by the presence of imaging artifacts. On the other hand, the giant cell flow

velocities found by Hathaway et al. (2013) may be underestimated due to averaging the moving and evolving flows at each point over the 10-13 days that point is visible in HMI data.

Numerical simulations for the three-dimensional radiative magnetohydrodynamics have progressed to the point that they now reproduce the appearance, the time evolution, and the emergent radiation associated with granules (Kitiashvili et al. 2012). We have compared our Doppler velocity spectrum with the spectrum calculated from the three-dimensional radiative hydrodynamics simulations obtained using the StellarBox code (Wray et al. 2015), which takes into account the effects of ionization, sub-grid-scale turbulence, internal structure and chemical composition. For analysis we used a fully developed hydrodynamic run in a slab 80 by 80 Mm in the horizontal, 25 Mm in depth below the photosphere, and 1 Mm of the atmospheric layer with the spatial grid resolution of 100 km. The photospheric velocity spectrum from this simulation (shown in Figure 13 by the blue line at high wavenumbers) is in very good agreement with the HMI Doppler velocity spectrum in the range of the spherical harmonic degree from 200 to 4000. However, the supergranulation bump is missing in these numerical simulations (as it was in the simulations of Stein et al. (2011)).

Understanding of the origin of supergranulation is still a significant challenge in solar physics. Origins based on the ionization of helium (Simon & Leighton 1964) or the collective interactions between downdrafts (Rast 2003) now seem unlikely based on numerical simulations. The supergranules are imbedded in the Sun’s surface shear layer (which extends to a depth of ~ 50 Mm) and are characterized by the magnetic network that forms around the periphery of each cell. Perhaps their origin lies with the influence of the Sun’s rotation or magnetic field on these convective flows.

The authors were supported by a grant from the NASA Living with a Star Program to Ames Research Center. The HMI data used are courtesy of the NASA/SDO and the HMI science teams. We gratefully acknowledge many useful discussions with Nagi Mansour, Alan Wray, Alexander Kosovichev, and Philip Scherrer.

REFERENCES

- Bray, R. J., Loughhead, R. E., & Durrant, C. J. 1984, *The solar granulation* (2nd edition)
- Chandrasekhar, S. 1961, *Hydrodynamic and hydromagnetic stability* (Oxford University Press)
- Couvidat, S., Rajaguru, S. P., Wachter, R., Sankarasubramanian, K., Schou, J., & Scherrer, P. H. 2012, *Sol. Phys.*, 278, 217
- Duvall, Jr., T. L. & Gizon, L. 2000, *Sol. Phys.*, 192, 177
- Hart, A. B. 1954, *MNRAS*, 114, 17
- Hathaway, D. H. 1982, *Solar Phys.*, 77, 341
- . 1987, *Solar Phys.*, 108, 1
- . 1992, *Solar Phys.*, 137, 15
- Hathaway, D. H., Beck, J. G., Bogart, R. S., Bachmann, K. T., Khatri, G., Petitto, J. M., Han, S., & Raymond, J. 2000, *Solar Phys.*, 193, 299
- Hathaway, D. H., Beck, J. G., Han, S., & Raymond, J. 2002, *Solar Phys.*, 205, 25
- Hathaway, D. H., Upton, L., & Colegrove, O. 2013, *Science*, 342, 1217
- Kitiashvili, I. N., Kosovichev, A. G., Mansour, N. N., Lele, S. K., & Wray, A. A. 2012, *Phys. Scr.*, 86, 018403
- Lawrence, J. K., Cadavid, A. C., & Ruzmaikin, A. A. 1999, *ApJ*, 513, 506
- Leighton, R. B., Noyes, R. W., & Simon, G. W. 1962, *ApJ*, 135, 474
- November, L. J., Toomre, J., Gebbie, K. B., & Simon, G. W. 1981, *ApJ*, 245, L123
- Rast, M. P. 2003, *ApJ*, 597, 1200
- Rieutord, M. & Rincon, F. 2010, *Living Reviews in Solar Physics*, 7, 2
- Rieutord, M., Roudier, T., Malherbe, J. M., & Rincon, F. 2000, *A&A*, 357, 1063
- Rieutord, M., Roudier, T., Rincon, F., Malherbe, J.-M., Meunier, N., Berger, T., & Frank, Z. 2010, *A&A*, 512, A4

- Scherrer, P. H., Schou, J., Bush, R. I., Kosovichev, A. G., Bogart, R. S., Hoeksema, J. T., Liu, Y., Duvall, T. L., Zhao, J., Title, A. M., Schrijver, C. J., Tarbell, T. D., & Tomczyk, S. 2012, *Solar Phys.*, 275, 207
- Schou, J., Borrero, J. M., Norton, A. A., Tomczyk, S., Elmore, D., & Card, G. L. 2012, *Sol. Phys.*, 275, 327
- Simon, G. W. & Leighton, R. B. 1964, *ApJ*, 140, 1120
- Simon, G. W. & Weiss, N. O. 1968, *ZAp*, 69, 435
- Stein, R. F., Lagerfjård, A., Nordlund, Å., & Georgobiani, D. 2011, *Sol. Phys.*, 268, 271
- Wachter, R., Schou, J., Rabello-Soares, M. C., Miles, J. W., Duvall, T. L., & Bush, R. I. 2012, *Sol. Phys.*, 275, 261
- Wray, A. A., Bensassi, K., Kitiashvili, I. N., Mansour, N. N., & Kosovichev, A. G. 2015, *ApJ* submitted